

Precipitation Processes in the Beta-Titanium Alloy Ti-5Al-5Mo-5V-3Cr

James Coakley^{a,b,*}, Vasilli A Vorontsov^c, Nicholas G Jones^a, Anna Radecka^c, Paul AJ Bagot^d, Kenneth C Littrell^e, Richard K Heenan^f, Frédéric Hu^c, Andrew P Magyar^g, David C Bell^g, David Dye^c

^aDepartment of Materials Science and Metallurgy, University of Cambridge, Cambridge CB3 0F3, England

^bDepartment of Materials Science and Engineering, Northwestern University, 2220 Campus Drive, Evanston, IL 60208-3108, USA

^cDepartment of Materials, Imperial College London, South Kensington, London SW7 2AZ, England

^dDepartment of Materials, University of Oxford, Oxford OX1 3PH, England

^eOak Ridge National Laboratory, Chemical and Engineering Materials Division, Oak Ridge, TN 37831 USA

^fRutherford Appleton Laboratory, Didcot, Oxon OX11 0QX, England

^gSchool of Engineering and Applied Sciences, Harvard University, Cambridge, MA, USA

Abstract

Precipitate evolution in Ti-5Al-5Mo-5V-3Cr-0.3Fe wt.% (Ti-5553) has been studied *in-situ* by small angle neutron scattering (SANS) during a two step ageing heat treatment of 300 °C/8 h + 500 °C/2 h. The first heat treatment step precipitates ω , with a corresponding increase in hardness of $\sim 15\%$ compared to quenched material. The second heat treatment step precipitates fine scale α from the ω phase, with a $\sim 90\%$ increase in hardness compared to quenched material.

The SANS measurements are complemented by atom probe tomography (APT) to give compositional information, *ex-situ* transmission electron microscopy (TEM) to confirm phase identification and size distribution locally, and X-ray diffraction (XRD) for additional confirmation of phase identification.

The ω phase is depleted in all the solute additions following 300 °C/8 h ageing heat treatment. The volume fraction of the ω phase from APT is estimated to be $\sim 7\%$. SANS modelling is consistent with disc shaped particles for the ω phase. The mean particle diameter increases from ~ 7.5 nm to 9.5 nm diameter between 1 h and 8 h heat treatment at 300 °C, while the thickness increases from ~ 4 nm to ~ 5 nm. The SANS model estimates the volume fraction to be $\sim 10\%$ for the 8 h heat treatment, using the phase compositions from APT.

Key words: Precipitation, titanium alloys, atom probe tomography (APT), transmission electron microscopy (TEM), small angle neutron scattering (SANS)

1. Introduction

Metastable β -Ti alloys are being increasingly employed in the aero-industry due to their extraordinary mechanical properties, namely a high strength to weight ratio and a good combination of toughness and fatigue resistance [1]. Ti-5Al-5Mo-5V-3Cr-0.3Fe wt.% (Ti-5553) is a recent β -Ti alloy employed in large section forgings in the Boeing 787 airframe [2].

Metastable β -Ti alloys are composed of a body-centered cubic (BCC) β matrix and hexagonal closed-packed (HCP) α particles in their stable state. These alloys generally lack nucleation sites for α , which combined with the high concentration of slow-diffusing solutes such as Mo, means that fully retained β microstructures can be realised. Like many of the β -Ti alloys, Ti-5553 forms a metastable ω phase when quenched from above the β transus [3, 4]. This is referred to as athermal ω phase (ω_{ath}). Subsequent low

temperature ageing below approximately 450 °C completes the formation of the hexagonal ω phase and it is generally stated that the element distribution evolves from the parent BCC β phase due to diffusion. This ω is distinguished as isothermal ω (ω_{iso}) [5]. Ti alloys that are lean in β stabilising elements may form a martensitic α' or α'' phase on quenching [6].

The high strength of β -Ti alloys is realised by the precipitation of fine α laths, on the order of 20 nm in width [7, 8]. The micron size primary α produced during conventional $\alpha + \beta$ forging does not contribute substantially to strength, but does act to pin β grain boundaries and prevent recrystallisation [9]. There is therefore a thread of work (*e.g.* [10, 11]) that aims to engineer the α nanostructure by using ω_{ath} as a metastable precursor to provide nucleation sites. It is then aged to a stable size and composition, at a temperature in the region of 300 °C (ω_{iso}). Finally, it is transformed to nanoscale α by ageing at temperatures around 500 °C. If this transformation sequence can be understood, the industrial prize is the realisation of stronger β -Ti alloys than can be manufactured in thick sections.

*Corresponding Author. Tel: +1 312 774 8634; fax: +1 847 467 2269

Email address: james.coakley@northwestern.edu (James Coakley)

Table 1: Heat treatments and corresponding nomenclature for the heat treatments employed on Ti-5553. All samples were initially heat treated above the β -transus followed by water quenching (WQ). The subsequent lower temperature heat treatments were followed by air-cooling (AC).

Label	Heat Treatment			
A-0	900 °C/0.5 h	WQ		
A-1	900 °C/0.5 h	WQ	300 °C/1 h	AC
A-2	900 °C/0.5 h	WQ	300 °C/2 h	AC
A-4	900 °C/0.5 h	WQ	300 °C/4 h	AC
A-8	900 °C/0.5 h	WQ	300 °C/8 h	AC
B-2	900 °C/0.5 h	WQ	300 °C/8 h	500 °C/2 h AC
C-1	900 °C/0.5 h	WQ	400 °C/1 h	AC
C-2	900 °C/0.5 h	WQ	400 °C/2 h	AC
C-4	900 °C/0.5 h	WQ	400 °C/4 h	AC
C-8	900 °C/0.5 h	WQ	400 °C/8 h	AC

It appears that fine-scale α nucleates either within the core of the ω precipitate, or in a depleted zone adjacent to the ω precipitate [3, 12]. It is generally believed that ω precipitation is detrimental to material properties and should be avoided as it is embrittling, for example [13].

This work aims to distinguish the extent of strengthening provided by α and ω phases in Ti-5553. *In-situ* small angle neutron scattering (SANS) was performed to study nanoscale particle evolution during a two step ageing heat treatment of 300 °C followed by a temperature hold at 500 °C. The SANS measurements are complemented by atom probe tomography (APT) to give compositional information, *ex-situ* transmission electron microscopy (TEM) to confirm phase identification and size distribution locally, and X-ray diffraction (XRD) for additional confirmation of phase identification. SANS is shown to be an excellent method for identifying ω precipitation. It is clarified that ω precipitation hardens Ti-5553, but not as significantly as the α phase. Finally, the microstructural parameters of the ω phase are fully quantified.

2. Experimental Details

The Ti-5553 forged billet used in this work has previously been studied and reported [4, 8]. All samples were prepared by initially heat treating Ti-5553 at 900 °C (~ 50 °C above the β transus [4]) for 30 min followed by water quenching. This initial condition is hereafter labelled A-0. The ageing conditions performed for study by a combination of TEM, XRD, APT and Vickers microhardness testing are presented in Table 1, along with corresponding nomenclature. All samples were air-cooled following the final heat treatments.

2.1. X-ray Diffraction (XRD)

The A-8 heat treated sample and the sample following *in-situ* SANS (sample B-2) were both measured in a laboratory XRD. The instrument used was a PANalytical X'Pert Pro MPD fitted with an X'celerator detector, using Cu-K α X-ray radiation with a characteristic wavelength of

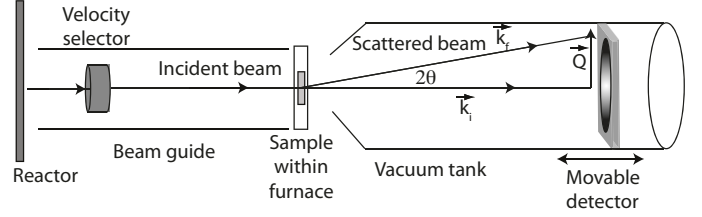


Figure 1: Schematic of the experimental arrangement used to perform pinhole small angle neutron scattering at HFIR, ORNL, Tennessee, USA.

1.541 Å at 40kV and 40mA current. Data were collected for 1 hour over a range of 20 - 100° 2θ . Phase identification was performed by comparison to powder patterns using CrystalDiffract software.

2.2. Transmission Electron Microscopy (TEM)

Specimens for TEM analysis were removed by spark-erosion and thinned using twin-jet electropolishing in a solution of 8 vol.% H $_2$ SO $_4$ in methanol at -40 °C and 18 V. TEM foils were examined using a JEOL JEM 2000FX microscope.

The ageing conditions studied in TEM were selected to aid the interpretation of the SANS experimentation. All microscopy was performed *ex-situ* at room temperature.

2.3. Small Angle Neutron Scattering (SANS)

SANS measures the shape and intensity of the coherent elastic scattering at small angles from the incident beam. The angles are much smaller than classical diffraction angles [14–21], typically under 5°. Pinhole SANS can provide scattering patterns from structures or fluctuations in composition or density on the length scale of about 1 to 100 nm, corresponding to the size of smaller precipitates in engineering alloys.

SANS was performed at the Oak Ridge National Laboratory (ORNL) High Flux Isotope Reactor (HFIR) on the General Purpose Small Angle Neutron Scattering (GP-SANS) instrument [22]. The set-up is illustrated in Figure 1. A mechanical velocity selector defined the incident neutron wavelength, in this case $\lambda = 4.75$ Å with a 10% spread, and the beam was collimated prior to the sample by a pair of apertures. \mathbf{k}_i is the incident wave vector with magnitude $k = 2\pi/\lambda$. The scattering vector \mathbf{Q} is the difference between incident and scattered wave vectors $\mathbf{Q} = \mathbf{k}_f - \mathbf{k}_i$. The magnitude of Q quantifies the lengths of the reciprocal space $Q = \frac{4\pi}{\lambda} \sin \theta$, where 2θ is the scattering angle.

A 10 mm square 1 mm thick sample of quenched Ti-5553 (A-0) was placed in a beam-line specific, argon gas atmosphere furnace and positioned in the beam-line. The sample to detector distance was set at 4 m, an aperture of 6 mm was used, and measurement count times were 900 s. The detector array was offset from the centre in order to measure a larger Q range.

119 The SANS raw data was reduced to absolute scattering
 120 ing cross section $\partial\Sigma(Q)/\partial\Omega$ using standard software in the
 121 HFIR Wavemetrics Igor package [22]. Data were corrected for:
 122 for: transmissions $T(\lambda)$ measured with the central beam
 123 stop removed and the incident beam attenuated, for back-
 124 grounds from the empty furnace, for dark current back-
 125 ground in the detector, and with the isotropic scattering
 126 from a 3 cm thick PMMA plate for detector pixel sensi-
 127 tivity variations. Data were placed on the absolute scale
 128 by the ratio of the area detector count rate to the beam-
 129 monitor count rate in the empty-beam transmission mea-
 130 surement for each wavelength.

131 Room temperature data were collected first, after which
 132 the furnace temperature was raised to 300 °C at $\sim 1^\circ\text{C}/\text{s}$
 133 and held at this temperature for 8 h while *in-situ* mea-
 134 surements were recorded every 15 minutes. After the 8 h
 135 thermal exposure the temperature was raised to 500 °C
 136 at $\sim 1^\circ\text{C}/\text{s}$ and held at this temperature for 2 h with the
 137 same measurement times.

138 2.4. Atom Probe Tomography (APT)

139 Atom probe tomography (APT) is a technique capa-
 140 ble of concurrently determining 3D material structure and
 141 chemical composition at the atomic scale, and is equally
 142 sensitive to all elements. Numerous detailed textbooks
 143 of the physical principles, sample preparation and APT
 144 experimental techniques are now available, for example
 145 [23, 24].

146 Needle-shaped atom probe samples of A-8 condition
 147 were prepared using the lift-out method on an FEI He-173
 148 lios NanoLab 600 DualBeamTM focused ion beam (FIB)
 149 system equipped with an OmniprobeTM. A detailed de-175
 150 scription of the FIB lift-out and tip sharpening procedure
 151 can be found elsewhere [25–27]. 176

152 APT experiments were performed in laser mode using
 153 a Cameca LEAPTM 4000X HR equipped with a 355 nm-178
 154 laser at Harvard University, USA, and LEAPTM 3000X HR-179
 155 with a 512 nm laser at the University of Oxford, UK. The-180
 156 tip temperatures were 40K and pulse energies of 0.05nJ-181
 157 (LEAP 4000X HR) and 0.2nJ (LEAP 3000X HR) were-182
 158 used. After data collection, runs were reconstructed util-183
 159 ising IVASTM data analysis software, using the estimated-184
 160 tip radius of the specimens from SEM imaging. 185

161 3. Results

162 3.1. Hardness Testing

163 Vickers micro-hardness test results for Ti-5553 in the-190
 164 quenched condition (A-0) and all heat treatments are pre-191
 165 sented in Figure 2. 1 h of heat treatment at 300 °C (sample-192
 166 A-1) resulted in an increase in hardness from ~ 280 to 310-193
 167 Hv. The hardness increased further to ~ 325 Hv with 7-194
 168 more hours heat treatment at 300 °C (sample A-8). When-195
 169 the temperature was ramped to 500 °C and held for two-196
 170 hours (condition B-2) there was a significant increase in-197
 171 hardness to ~ 515 Hv. Separate experiments showed that-198

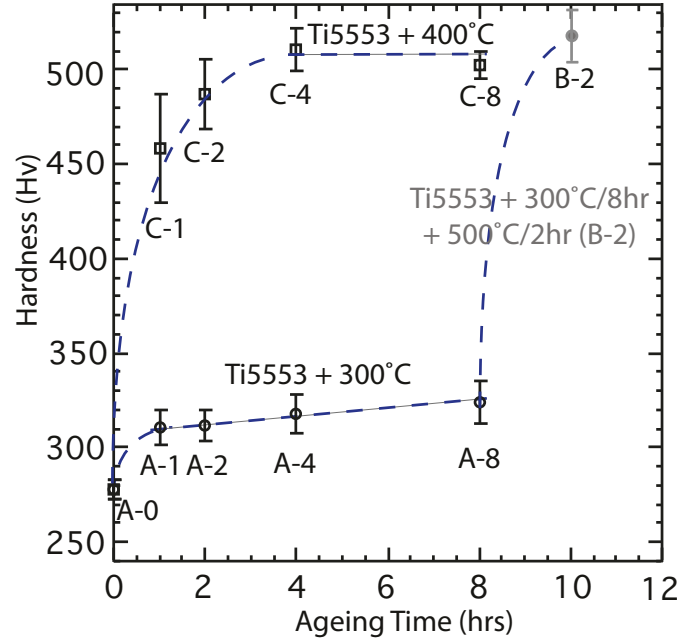


Figure 2: Evolution of Vickers micro-hardness of Ti-5553 as a function of ageing time. The data presented shows the hardness of the quenched material (A-0), 300 °C and 400 °C samples with ageing times between 1 and 8 h, labelled A-1 to A-8 and C-1 to C-8 respectively. The hardness of sample B-2 which received a 300 °C/8 h + 500 °C/2 h ageing heat treatment is also presented. Trendlines have been inserted to the data as a guide to the eye.

ageing at 400 °C for 1 h (sample C-1) resulted in a large hardness increase from ~ 280 to 460 Hv, and a further 7 hours thermal exposure increased the hardness to ~ 500 Hv (sample C-8).

186 3.2. X-ray Diffraction

187 The XRD profiles for sample A-8 and B-2 are presented
 188 in Figures 3a and b respectively. The lattice constants of
 189 α and β for Ti-5553 were previously determined [8] and
 corresponding peak positions are presented in Figure 3.
 The peak positions based on ω in pure Ti [28] and α''
 in the β -Ti alloy Ti-2448 [29] are also shown.

The doublets observed in the β matrix peaks in Figure 3a are due to diffraction arising from both $K_{\alpha 1}$ and $K_{\alpha 2}$ emissions. The diffraction patterns of the two heat treatments are markedly different, with sample B-2 exhibiting much broader peaks than A-8. There are numerous microstructural effects that can result in broad diffraction peaks, for example dislocations, twinning and coherency strains. In this case it is presumably related to the nanometer scale of the alpha particles by the Scherrer equation.

A number of low intensity peaks have not been labelled as one cannot definitively determine the corresponding diffracting crystal structure. A clear peak at 44.4° in Figure 3a is evidence of extensive ω precipitation (labelled ω (020)) in sample A-8. This peak is not present in B-2 (Figure 3b). The peak at 35.5° of the same figure may

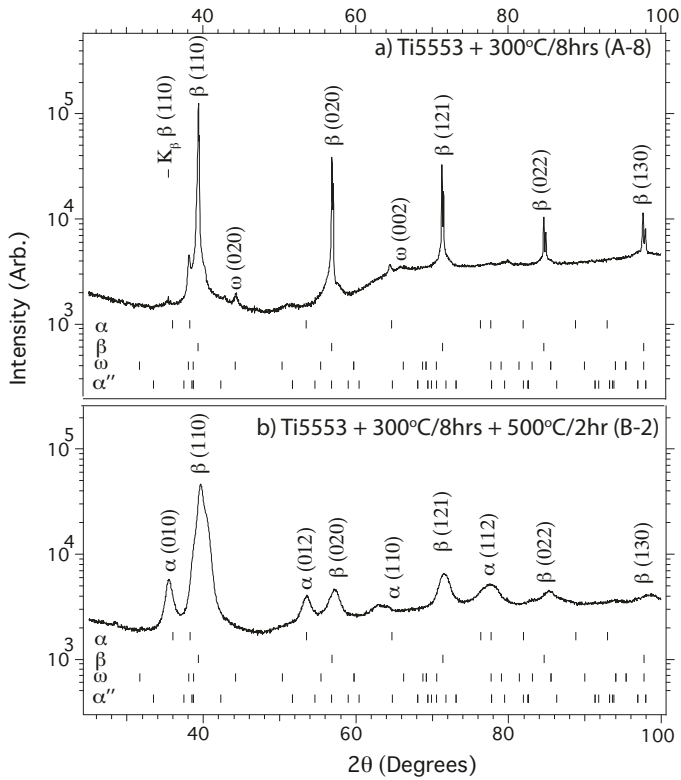


Figure 3: X-ray diffraction patterns for a) 300 °C/8 h and b) 300 °C/8 h + 500 °C/2 h heat treated samples.

199 arise from the Cu K_{β} (011) $_{\beta}$ position which has not been
200 completely removed with the secondary monochromator.

201 Strong peaks at 35.4°, 53.2° and 77.7° are evidence of
202 extensive α precipitation in sample B-2, Figure 3b.

203 3.3. Transmission Electron Microscopy (TEM)

204 Figure 4 shows the evolution of the TEM diffraction
205 patterns during thermal exposure along with correspond-
206 ing dark field images and two schematic diagrams to aid
207 analysis. All the diffraction patterns are viewed parallel
208 to the [113] zone axis for all the samples. B-2 is the sample
209 following the SANS experiment. It is reasonable to assume
210 that the microstructure at room temperature is represen-
211 tative of the microstructure at 300 °C, as it is well below
212 the β transus temperature of ~ 845 °C for Ti-5553 [4].

213 The streaking along the $\langle 112 \rangle_{\beta}$ in the initial condi-
214 tion TEM diffraction pattern (Figure 4a) is associated with
215 ω_{ath} [3, 12]. The very faint spots at $1/2 \langle 112 \rangle_{\beta}$ are reflec-
216 tions from α'' phase. These were most obvious in sample
217 A-0. Distinct spots were seen to form in the diffraction
218 patterns and grow in intensity at $1/3$ and $2/3 \langle 112 \rangle_{\beta}$
219 with increasing thermal exposure times up to 8 h. These
220 spots correspond to the ω_{iso} phase. There were no obvi-
221 ous reflections due to the α phase in any of the diffraction
222 patterns of the 300 °C heat-treated samples. The TEM
223 diffraction pattern of sample B-2 (Figure 4j) was markedly
224 different to samples A-1 to A-8. There were clear strong
225 α reflections which can be identified using the schematic

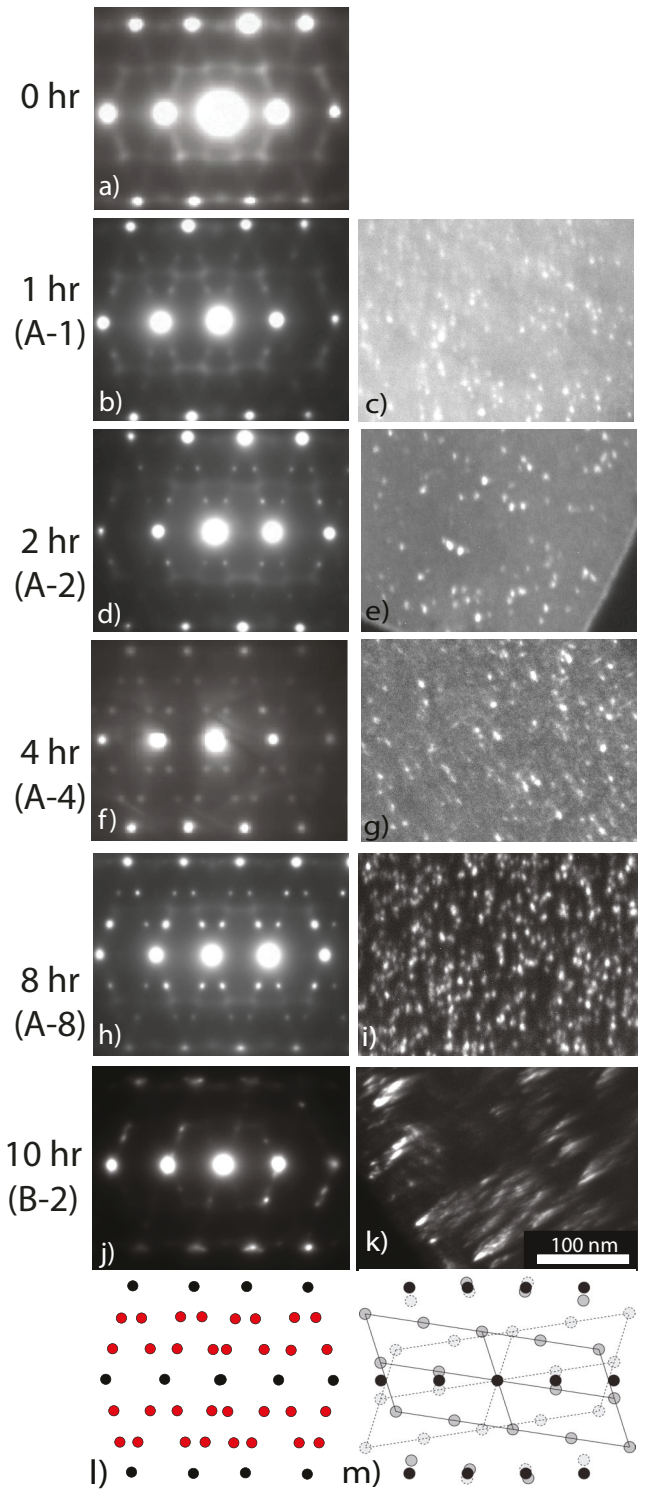


Figure 4: a-k) TEM diffraction pattern evolution and associated dark field imaging for samples with ageing times of 0 h – 8 h at 300 °C (samples A-0 to A-8) and 300 °C/8 h + 500 °C/2 h, (sample B-2). All diffraction patterns are viewed parallel to the [113] zone axis. Dark field images are taken from the $1/3 \langle 112 \rangle$ reflection associated with the ω phase. l) Schematic illustrating the position of diffraction spots due to the ω phase (black: β spots; red: ω spots) and m) the α phase (black: β spots; light and dark grey: α spots).

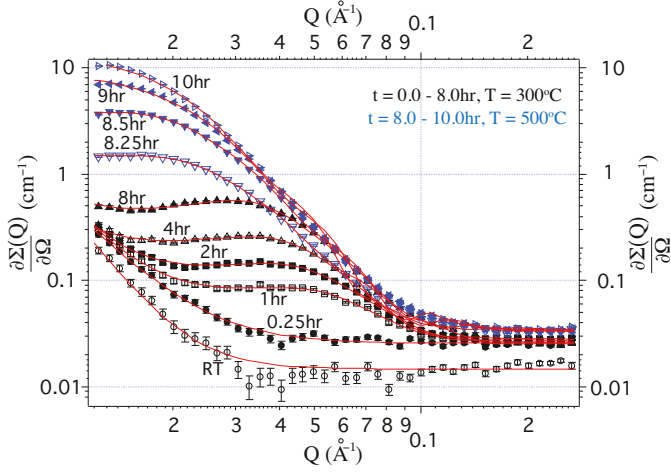


Figure 5: The evolution of Ti-5553 SANS scattering curves with time measured at room temperature (RT) and *in-situ* at 300 °C for 0–8 h, after which the temperature was ramped to 500 °C, plotted on a log-log scale. The times represents the time at which the measurement was finished, with each measurement taking 0.25 h. Solid lines represent model fits based on monodisperse disc-shaped particles.

(m), and the reflections associated with ω were fully or almost fully removed compared to (h).

It was not possible to obtain dark field images from the reflections at $1/3$ and $2/3 \langle 112 \rangle_{\beta}$ in the initial condition, however the micrographs produced from an ω reflection for the samples A-1 to A-8 and B-2 are shown, Figure 4. It is apparent that ω particles were of elliptical morphology when viewed in 2D with diameter $\sim 5-10$ nm. The volume fraction appeared to increase with thermal exposure at 300 °C up to 8 h, however foil thickness can influence the observed volume fraction. The dark field image of sample B-2 (Figure 4k) showed much larger particles.

3.4. Small Angle Neutron Scattering

The sample scattered neutrons quite isotropically at room temperature and all elevated temperature measurements. This was deduced from analysis of the neutron counts in the 2D detector. The data for each measurement was azimuthally averaged, and the evolution of the fully reduced scattering curves with thermal exposure time are presented in Figure 5, plotted as absolute scattering cross-section $\partial\Sigma(Q)/\partial\Omega$ (commonly referred to as intensity) against the magnitude of the scattering vector Q .

The room temperature measurement and first elevated temperature measurement showed no obvious scattering from nanoscale particles within the measured range of Q , Figure 5. From TEM it was known that ω_{ath} is initially present (Figure 4a). Therefore scattering arising due to ω_{ath} may be apparent at a Q range outside that measured in this work, or there may be no scattering arising from this phase if the ω_{ath} phase composition was the same as the matrix. After 1 h of thermal exposure a broad peak was seen forming at $\sim 0.043 \text{ \AA}^{-1}$, which grew in intensity

Table 2: Nominal composition and the compositions of Ti-5553 measured by inductively coupled plasma optical emission spectrometry (ICP-OES) and by atom probe tomography (APT) for the bulk material. The APT samples have received a +300 °C/8 h heat treatment. The subscripts 1 and 2 refer to needle 1 and needle 2, which were measured on LEAP 4000X HR and LEAP 3000X HR instruments respectively. All compositions are in atomic %.

Bulk Composition, at.%	Ti	V	Fe	Al	Mo	Cr
Nominal Composition	81.1	4.7	0.3	8.8	2.5	2.7
ICP-OES [4]	80.8	4.9	0.3	8.7	2.6	2.7
APT ₁	80.6	5.1	0.2	8.5	1.7	3.2
APT ₂	81.1	5.2	0.3	8.4	1.8	2.8

and shifts to lower Q with increasing ageing time, with a peak position of $\sim 0.028 \text{ \AA}^{-1}$ after 8 h.

After 8 h at 300 °C the temperature was ramped to 500 °C and the scattering curve shape and intensity changed dramatically. After 8.25 h the intensity was lower than after 8 h in the Q range of $0.037-0.043 \text{ \AA}^{-1}$. The intensity at low Q increased with thermal exposure time at 500 °C and appeared to plateau at the lowest values of Q . Modelling is required in order to deduce information of particle size, shape and volume fraction from SANS measurements.

3.5. Atom Probe Tomography

Two APT measurements are presented in this work, referred to as needle 1 and needle 2 respectively. Both needles were prepared from the A-8 heat treated condition.

The two needles were analysed in separate LEAP systems equipped with different laser pulse wavelengths, in order to ensure any segregation behaviour was not a result of laser-artefacts. Datasets containing 56 million and 51 million ions for needles 1 and 2 were obtained respectively. The bulk compositions determined by APT are in excellent agreement with those previously determined by inductively coupled plasma optical emission spectrometry (ICP-OES) [4], Table 2. APT reconstructions are presented in Figure 6, showing 3nm thick slices through the entire datasets. Along with good agreement between needles 1 and 2 in terms of compositions, Figure 6 reveals the microstructures are very similar, with dense dispersions of small (<10 nm diameter) precipitates throughout. The precipitates are highlighted by Ti 86.5 at.% isosurfaces, thus in comparison to the bulk they are enriched in Ti. The similarity in compositions between matrix and precipitates for the main element, Ti, prevented the use of clustering algorithms to isolate the latter, but the isosurfaces employed in both needles 1 and 2 enable generation of proxigrams to examine in detail changes in chemistry.

Proxigrams of A-8 are presented in Figure 7, averaging across (i) 687 precipitates and (ii) 819 precipitates. The chemical interface width was approximately 4 nm. The solute additions were rejected from the precipitates, resulting in Ti enriched particles. The average Ti concentration within the isosurface of the particles was approximately 10 at.% more than the matrix. The cores of the precipitates are the regions of highest Ti enrichment. These cores are

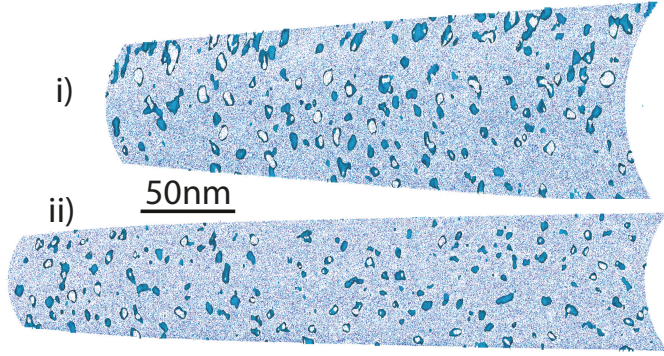


Figure 6: APT reconstructions of a Ti 86.5 at.% isosurface on a 3nm thick slice through the whole map for Ti-5553+300 °C/8 h needles. i) Needle 1 was measured on a LEAP 4000X HR and ii) needle 2 was measured on a LEAP 3000X HR. Al (blue) and V (purple) are shown only, for clarity.

301 14 at.% higher in Ti concentration than the matrix. The Ti
 302 composition of the matrix was depleted by ~ 1 at.% com-
 303 pared to the bulk composition. The concentration of all
 304 solute additions combined was approximately four times
 305 higher in the matrix than in the precipitates.

306 4. Discussion

307 4.1. Atom Probe Tomography

308 APT has previously been applied to the study of precipi-
 309 tation in Ti-5553 by Nag *et al.* [3, 11]. They could
 310 not discern precipitation in Ti-5553 aged at 400 °C/2h by
 311 APT, and attributed this to the low diffusivities of the
 312 elements at this temperature [11]. Nag *et al.* also pub-
 313 lished APT results identifying ω and α precipitates in Ti-
 314 5553 aged at the lower temperature of 350 °C/2h [3]. The
 315 phases were distinguished based on solute addition com-
 316 positional profiles that fluctuate within ± 1 at.% [3].

317 The two proxigrams presented in this work are from
 318 687 and 819 identified particles, and show a very clear and
 319 significant decrease in all solute additions within the precipi-
 320 tates. Based upon the corresponding TEM (Figure 4h
 321 & i) for Ti-5553 aged at 300 °C/8 h it is reasonable to
 322 identify these precipitates as the ω phase. It is of particu-
 323 lar significance that the ω phase is depleted in Al. It is
 324 debated in the literature whether α precipitates nucleate
 325 from within the ω precipitates, at the ω/β interface, or
 326 whether the ω precipitates undergo a solid state transfor-
 327 mation to form the α precipitates [12, 30–36]. Given that
 328 Al is the primary α stabiliser in this alloy, it seems un-
 329 likely that it would nucleate in an ω core so depleted in
 330 this element. It is more logical that α would precipitate
 331 at the ω/β interface where there is slight Al enrichment,
 332 which is the precipitation mechanism proposed by Nag *et al.*
 333 [3]. APT studies of longer ageing times are required in
 334 order to be definitive.

335 Using a straightforward atom count analysis of needle
 336 1 gives an ω volume fraction of approximately 7% in the

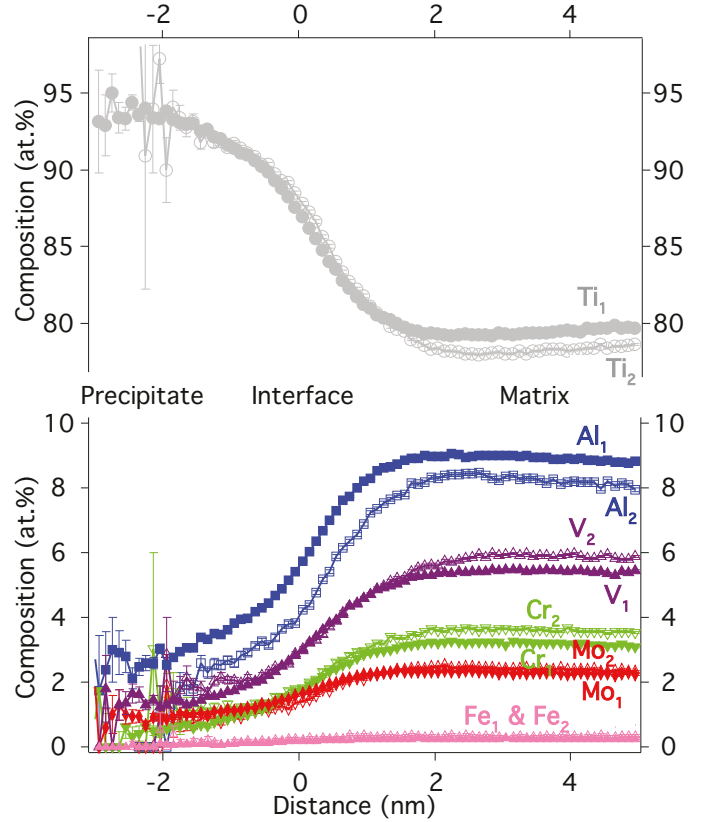


Figure 7: Proxigrams of Ti-5553 +300 °C/8 h (A-8) heat treatment averaged through identified precipitates in LEAP 4000X HR (subscript 1) and in LEAP 3000X HR (subscript 2).

APT data (needle 2 yields a fraction of 4%, which while comparable is from the lower mass-resolution on the 3000X HR). Considering the error in atomic fractions if the lever rule is applied $n_{i,error} = (n_{i,ppt}\phi + n_{i,matrix}(1-\phi)) - n_{i,bulk}$, where n_i is the atomic fraction of element i in the precipitate, matrix, or bulk, and ϕ is the precipitate volume fraction, the error is small. The maximum error in atomic fraction is less than 0.1 at.% for Ti, Al and V, 0.2 at.% for Cr, and 0.5 at.% for Mo, when the volume fraction of 7% is introduced to the equation.

4.2. Transmission Electron Microscopy

The TEM study shows the progressive development of ω spots when heat-treated at 300 °C. Imaging in dark field indicates an increase in volume fraction of the nanoscale precipitates, Figure 4, however this can be influenced by foil thickness. Nag *et al.* previously performed TEM on a Ti-5553+350 °C/2 h heat-treated sample, and the difference in the extent of precipitation between their 350 °C heat treatment, and the 300 °C heat treatment performed in this work is dramatic [3]. Their sample exhibited very strong α and ω reflections after 2 h heat treatment. In this work there are no α reflections after 300 °C/2 h heat treatment (4d), and the ω reflections are very weak in comparison to those presented by Nag *et al.* [3].

Sample B-2, which has had the additional exposure of 500 °C/2h, shows a significant decrease in intensity from the ω reflections, to the point that they may have been totally removed. The α reflections are now clearly present after this heat treatment, Figure 4j. This indicates that ω has gone into dissolution if one does not recognise the ω to α transformation, however this transformation is the alternative interpretation [8].

4.3. X-ray Diffraction

It is clear that ω is present after 300 °C/8 h heat treatment, Figure 3. The XRD pattern is dramatically different following the 500 °C/2h thermal exposure, with no apparent ω reflections and strong α peaks present. This agrees well with the TEM observations. Due to the low intensity of ω reflections they can be difficult to distinguish from background in laboratory XRD, so care should be taken with its application. It is for this reason that TEM diffraction is the primary analysis tool for β -Ti alloy precipitation studies.

4.4. Small Angle Neutron Scattering

The SANS data show a scattering peak forming during thermal exposure due to precipitation, Figure 5. However in order to deduce microstructural parameters such as particle size, shape and volume fraction, modelling is required. The model applied should be based on complementary microscopic analysis, such as the TEM study in this work. *In-situ* SANS was recently applied to the study of precipitation at 400 °C in the β -Ti alloy, Gum metal, with different processing conditions [37]. The scattering curves in this work show similar shape to the cold-rolled Gum metal, however the analysis of cold-rolled Gum metal was confounded by co-precipitation of the α phase. As the ω particles appear to be circular in the TEM imaging as was the case for Gum metal, the SANS model for disc-shaped particles previously developed is applied to the Ti-5553 SANS data of this work [37].

The SANS model employed in this work is described elsewhere in extensive detail [37], and is summarised here. The model was developed in the FISH software package [38] and fits to the data by a least squares refinement. Although the model fits well to the data, Figure 5, it may not be a unique solution. Disc-shaped particles for ω are reasonable based upon the TEM and APT. A model using elliptical particles rather than discs also fitted to the data, and the fitting parameters of both models were in good agreement with the exception of the disc radius and larger elliptical radius. The model elliptical radius was slightly smaller than the model disc radius. The residual error between data and model fit was larger for the ellipse model.

The disc model defines the probability of small angle scattering (SAS) from non-dilute uniform monodisperse discs as

$$\partial\Sigma(Q)/\partial\Omega = NV^2(\Delta\rho)^2P(Q)_{\text{Discs}}S(Q)_{\text{HS}} + aQ^{-n} + \text{BKG} \quad (1)$$

where $P(Q)_{\text{Discs}}$ is the form factor or shape function of the disc shaped particles. $P(Q)$ depends on the size and shape of the particle and is normalised such that $P(Q = 0) = 1.0$ [39]. The form factor has an associated impenetrable hard sphere structure factor $S(Q)_{\text{HS}}$ [40]. The structure factor is required at higher volume fractions to account for the interference from waves scattered by adjacent particles. BKG is a small flat background to account for incoherent scattering, and aQ^{-n} accounts for scattering from the precipitate/matrix interface. N is the number of particles per unit volume, V is the volume of one particle. Note that the dispersed particle volume fraction $\phi = NV$. $\Delta\rho = \rho_{\text{ppt}} - \rho_{\text{matrix}}$ is the neutron scattering length density difference between the particle and its matrix. The scattering length density of phase x is

$$\rho_x = (\rho_{\text{mass}}N_A/M_r)\Sigma n_i b_i \quad (2)$$

where ρ_{mass} is the phase mass density, N_A is Avogadro's number, M_r is the relative molecular weight of the phase, n_i is the atomic fraction of element i in the phase, and b_i is that element's associated neutron scattering length. Element partitioning between phases (which can be quantified by APT) will typically cause a neutron scattering length density difference. Therefore precipitates of different composition to the matrix can be identified by small angle scattering.

$P(Q)_{\text{Discs}}$ has three fitting parameters: scale (a fitting parameter particular to FISH equal to $\phi(\Delta\rho)^2$), disc diameter D , and disc length L . If the scattering contrast $(\Delta\rho)^2$ is known, the volume fraction ϕ can be determined from the $\phi(\Delta\rho)^2$ term. $S(Q)_{\text{HS}}$ has two fitting parameters, the hard sphere diameter D_{HS} and the hard sphere volume fraction V_{HS} . Though this may be an effective approximation for non-spherical particles, the hard sphere volume fraction should be similar to ϕ in a good fit. The final fitting parameters are a and n . For fits to the 300 °C data, n fitted to ~ 4 for early time measurements where a large linear region was present in the data at low Q , and so n was then constrained at this value. This is standard Porod scattering and is presumably associated with scattering from the grains rather than nanoparticles. For fits to the 500 °C data there was no linear region to fit so a was put to zero. Thus, the model is composed of 10 fitting parameters in total. Initial estimates of these parameters are introduced into the model, and the model fit converges to the least squares minimum with the data by the Marquadt method.

The model results for ω particle diameter, length and $\phi(\Delta\rho)^2$ are presented in Figure 8. The errors from the fitting routine are not included, but are of the order of 0.1 nm for particle length and radius, and $0.01 \times 10^{-10} \text{cm}^{-1}$ for $\phi(\Delta\rho)^2$. During the 300 °C/8 h heat treatment the ω particle mean diameter increases from 7.5 – 9.5 nm, in good agreement with TEM, and the length increases from 4–5nm. Following the temperature ramp to 500 °C the applicability of a unimodal disc-shaped model may be questionable, as it is known that the α phase grows as nanoscale

laths on ageing of quenched Ti-5553 at 570 °C [8]. The two phase disc model fits the data well, and the results are presented. Interestingly, the results still show agreement with TEM, the discs grow in diameter to ~ 20 nm and length to ~ 8 nm. These dimensions are similar to the width of the α laths in the work of Jones *et al.* [8]. A rod model is a logical approach to fit for an acicular α lath structure. Therefore the disc model was reapplied and fitted to the data, but with $L > D$. The fits were very poor, giving argument that the scattering is arising from nanoscale α particles that are still of disc shape ($D > L$).

Subtracting the hard sphere diameter from either the particle diameter or length should give an approximation to an interparticle distance of the system. Following the 300 °C/8 h $D_{HS} \sim 16$ nm, giving an interparticle distance, $\lambda_d \sim 7.5$ nm which seems reasonable based on TEM (Figure 4i).

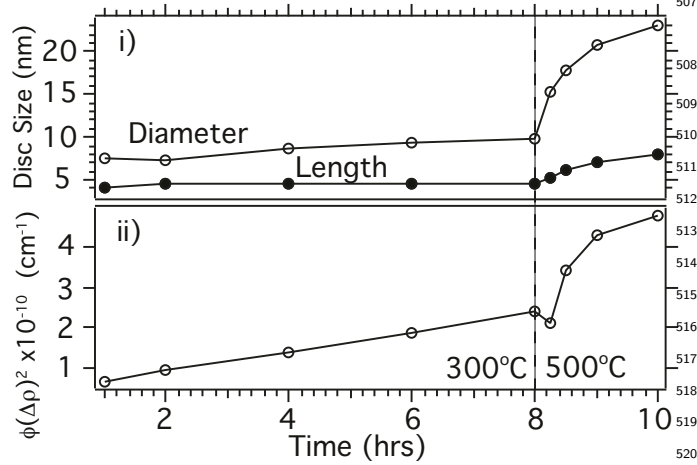


Figure 8: Model parameter results from fits to the measured SANS data for i) particle size, and ii) $\phi(\Delta\rho)^2$ term.

The neutron scattering length densities of β and ω following the 300 °C/8 h heat treatment are $\rho_\beta = -1.3 \times 10^{10} \text{cm}^{-2}$ and $\rho_\omega = -1.7 \times 10^{10} \text{cm}^{-2}$ respectively, giving a scattering length density contrast of $\rho_\omega - \rho_\beta = -0.4 \times 10^{10} \text{cm}^{-2}$. These values are calculated from Eqn. (2), by: (i) calculating each phase mass density ρ_{mass} and molecular weight M_r from first principles based on the atomic weights and densities of each element in each phase and the atomic fraction in each phase determined in this work by APT; and (ii) using previously published scattering lengths of each element [41]. The compositions used for each phase were determined from the proxigram (needle 1, Figure 7), away from the interfacial region. As the scattering length density difference $\Delta\rho = \rho_\omega - \rho_\beta$ is now known, the volume fraction can be deduced from the value of the SANS model fitting parameter $\phi(\Delta\rho)^2$ (Figure 8). The volume fraction from SANS after 300 °C/8 h is approximately 10%, in reasonable agreement to the 7% determined by APT. There is further agreement with the SANS model hard sphere volume fraction term $V_{HS} = 12\%$ for the same heat treatment. As a crude first approximation,

if one assumes that the composition is constant during the 300 °C heat treatment, then the volume fractions are $\sim 3\%$, 4% , and 6% after 1 h, 2 h, and 4 h heat treatments respectively.

4.5. Hardness Testing

From the detailed microstructure analysis performed, it is not difficult to attribute the material properties to the precipitation process. The precipitation of ω phase at 300 °C (A-8) corresponds to an increase in hardness of about 40Hv over the 8 h heat treatment. This represents a $\sim 15\%$ increase in hardness compared to the quenched material. The subsequent age at 500 °C (B-2) increased the hardness by a further ~ 200 Hv, which is an increase of $\sim 90\%$ from the quenched material. This corresponds to the precipitation of α phase. The ageing at 400 °C shows similar hardness to the two-step ageing heat treatment, and so is presumably precipitating nanoscale α phase.

4.6. Summary of Techniques

TEM has been the primary analysis tool for the study of ω , and by comparison of techniques it is clear why. It allows both crystallographic determination and two dimensional imaging. Laboratory XRD gives some initial insight to precipitation, however the ω peaks tend to get lost in the background. In Figure 3a, there is an indication that ω is present based on a single low intensity peak labelled as ω (020). This is not enough to be conclusive. Small angle scattering (SAS) detects early nucleation of ω most readily of all the techniques. The modelling of SAS data is not trivial, and requires complementary microscopy. APT is unrivalled in terms of quantifiable capabilities, but this work illustrates that measuring the earliest stages of precipitation is far from simple. The authors did not manage to quantify the precipitation that occurred following 300 °C/2 h ageing heat treatment, which has been identified by SANS and TEM. This may be a limitation of the detection efficiency, which is $\sim 37\%$ on both current generation instruments used.

5. Conclusions

5.1. Transmission Electron Microscopy and X-ray Diffraction

The volume fraction of ω phase in Ti-5553 appears to increase with thermal exposure time, when held at 300 °C for 8 h. A subsequent age of 500 °C/2 h precipitates α phase. The ω phase is removed.

5.2. Atom Probe Tomography

APT of the 300 °C/8 h material shows that the ω precipitates possess an atomic composition of approximately 94 at.% Ti, 14 at.% higher than the bulk composition, towards the core of the precipitate. The average Ti composition within the isosurface is approximately 10 at.% higher than the bulk composition. The precipitates are

depleted in all solute additions including Al. This is significant as Al is an α stabiliser, thus it is unlikely that α will subsequently nucleate from an ω core. It seems more reasonable that it will nucleate at the ω/β interface which is an area of slight Al enrichment. This has previously been proposed by Nag *et al.* [3].

5.3. Small Angle Neutron Scattering

In-situ SANS was performed on a sample of Ti-5553 during a two step ageing heat treatment of 300 °C/8 h + 500 °C/2 h. A SANS model of disc-shaped particles fits the data well, and is supported by TEM and APT. The ω particles grow to a diameter of ~ 10 nm and the length remains approximately constant between $\sim 4 - 5$ nm during the 300 °C/8 h heat treatment.

The volume fraction of ω following 300 °C/8 h heat treatment is $\sim 7\%$, based on atom counts in the APT analysis. Using the APT phase composition results as input to the SANS model gives a volume fraction of $\sim 10\%$.

5.4. Hardness Testing

Hardness testing shows that the ω phase increases the hardness of the alloy by $\sim 15\%$, while the α phase increases the hardness by $\sim 90\%$.

Acknowledgements

The authors would like to acknowledge funding from EP SRC under grant EP/H0004882/01. VAV and JC would like to acknowledge support from the EPSRC doctoral prize fellowship and Marie Curie fellowship respectively. This work utilizes the Oak Ridge National Laboratory's High Flux Isotope Reactor which is sponsored by the Scientific User Facilities Division, Office of Basic Energy Sciences, U.S. Department of Energy. JC would like to thank R Chater for providing training in FIB milling and his helpful discussions. For the APT analysis, T.L. Martin is thanked for assistance with running samples and M.P. Moody for helpful discussions. PAJB acknowledges support from The Queen's College Oxford for experiments performed at Harvard University, USA.

References

- [1] Bania PJ JOM 1994;46(7):16
- [2] Boyer RR & Briggs RD JMEPEG 2005;14:681
- [3] Nag S, Banerjee R, Srinivasan R, Hwang JY, Harper M, Fraser HL. Acta Mater 2009 57:2136
- [4] Jones NG, Dashwood RJ, Dye D, Jackson M Mater Sci & Eng A 2008;490:269
- [5] Williams JC In: Jaffee RI & Burte HM *et al.* eds., Ti1973 Science and Technology. Plenum Press, New York USA. 1973:1433-1494
- [6] Lütjering G & Williams JC Titanium. Springer-Verlag, Berlin Heidelberg New York. 2003
- [7] Raghunathan SL, Stapleton AM, Dashwood RJ, Jackson M, Dye D. Acta Mater 2007 55:6861
- [8] Jones NG, Dashwood, R.J. Jackson M, Dye D Acta Mater 2009; 57:3830
- [9] Duerig TW, Williams JC. In: Boyer RR, Rosenberg HW, eds., AIME, New York, USA, 1984:19-67
- [10] Nag S *et al.* Phys Rev Lett 2011 106:245701
- [11] Nag S, Banerjee R, Hwang JY, Harper M, Fraser HL. Phil Mag 2009 89(6):535
- [12] Nag S, Banerjee R, Fraser HL. J Mater Sci 2009;44:808
- [13] Bowen AW Scr Met 1971;5(8):709
- [14] Coakley J, Reed RC, Warwick JLW, Rahman KM, Dye D. Acta Mater 2012;60:2729
- [15] Stone HJ, Holden TM, Reed RC. Acta Metall 1999;47:4435
- [16] Ma S, Rangaswamy P, Majumdar BS. Scr Mater 2003;48:525
- [17] Ma S, Brown D, Bourke MAM, Daymond MR, Majumdar BS. Mater Sci Eng A 2005;399:141
- [18] Daymond MR, Preuss M, Clausen B. Acta Mater 2007;55:3089
- [19] Preuss M, da Fonesca JQ, Grant B, Knoche E, Moat R, Daymond M. In: Reed RC, Green KA, Caron P, Gabb TP, Fahrman MG, Huron ES, Woodard SA, eds., Superalloys 2008. TMS, PA, 405-414
- [20] Dye D, Coakley J, Vorontsov VA, Stone HJ, Rogge RB. Scr Mater 2009;48:525
- [21] Coakley J, Dye D. Scri Mater 2012;67:435
- [22] Wignall GD, Littrell KC, Hetter WT, Melnichenko YB, Kailey KM, Lynn GW, Myles DA, Urban VS, Buchanan MV, Selby DL, Bulter PD J Appl Cryst 2012;45:990
- [23] Miller MK. Atom Probe Tomography: Analysis at the Atomic Level, Kluwer Academic. New York, USA. 2000
- [24] Gault RB, Moody MP, Cairney JM, Ringer SP. Atom Probe Microscopy, Springer. New York, USA. 2006
- [25] Thompson K. *et al.* Ultramicroscopy 2007;107:131
- [26] Cerezo A *et al.* Materials Today 2007;10(12):36
- [27] Kelly TF & Larson DJ. Mater Char 2000;44:59
- [28] Jamieson JC Science 1963;140:72
- [29] Liu JP *et al.* Sci Rep 2013 3:2156
- [30] Blackburn MJ, Williams JC. Trans Met Soc AIME 1968 242:2461
- [31] Pennock GM, Flower HM, West DRF. Titanium 1980: Science and Technology 1343
- [32] Furuhashi T, Maki T, Makino T. J Mater Proc Technol 2001 117:318
- [33] Hickman BS J Inst Met 1968 96:330
- [34] Langmayr F, Fratzl P, Vogl G. Phys Rev B 1994 49(17):11759
- [35] Azimzadeh S, Rack HJ. Metall Mater Trans A 1998;29:2455
- [36] Prima F, Vermaut P, Texier G, Ansel D, Gloriant T. Scripta Mater 2006;54:645
- [37] Coakley J, Vorontsov VA, Littrell KC, Heenan R, Ohnuma M, Jones NG, Dye D. J Alloy Compd 2015 623:146
- [38] Heenan RK. RAL Report 1989;89
- [39] King SM. In: Pethrick RA, Dawkins JV, eds., Modern techniques for polymer characterisation. Wiley, Chichester, 1999:171-232
- [40] Ashcroft NW, Lekner J. Phys Rev 1966;145:83
- [41] Kline SRJ. J Appl Cryst 2006;39(6):895
- [41] Sears VF. Neutron News 1992;(3)3:26